

Multiple Floquet Chern insulator phases in the spin-charge coupled triangular-lattice ferrimagnet: Crucial role of higher-order terms in the high-frequency expansion

Rintaro Eto  and Masahito Mochizuki *Department of Applied Physics, Waseda University, Okubo, Shinjuku-ku, Tokyo 169-8555, Japan*

(Received 8 April 2024; revised 23 July 2024; accepted 24 July 2024; published 8 August 2024)

We study the effects of photoirradiation with circularly polarized light on the Dirac half-metal state induced by the ferrimagnetic order in a triangular Kondo-lattice model. Our analysis based on the Floquet theory reveals that two types of Floquet Chern insulator phases appear as photoinduced nonequilibrium steady states and that these two phases can be experimentally detected and distinguished by measurements of the Hall conductivity. It is elucidated that these rich nonequilibrium topological phases come from higher-order terms in the high-frequency expansion called Brillouin-Wigner expansion, which is in striking contrast to usually discussed Floquet Chern insulator phases originating from the lowest-order terms of the expansion. So far, the lattice electron models on simple nonmultipartite lattices such as triangular lattices and square lattices have not been regarded as targets of the Floquet engineering because the lowest-order terms of the high-frequency expansion for Floquet effective Hamiltonians cancel each other to vanish in these systems. Our findings of the Floquet Chern insulator phases in a triangular Kondo-lattice model are expected to expand the range of potential models and even materials targeted by the Floquet engineering.

DOI: [10.1103/PhysRevB.110.085117](https://doi.org/10.1103/PhysRevB.110.085117)

I. INTRODUCTION

Since the first theoretical proposal of the Floquet Chern insulator state in graphene [1,2], the Floquet engineering of topology in condensed matters has been a central issue of the photoinduced physics [3,4]. A recent experiment [5] and a precise theoretical analysis [6] indicate that, although the experimentally observed photoinduced transverse current in graphene is largely coming from the electron population imbalance around the Dirac cone, there is tiny but finite contribution from photoinduced Berry curvatures. Possible realizations of the Floquet Chern insulator state are theoretically and experimentally proposed also in several atomic-layer systems including twisted multilayer graphene [7–9], silicene [10], black phosphorene [11], transition-metal dichalcogenides [12–15], organic salts [16–22], and cuprate superconductors [23]. In addition, subsequent seminal works have revealed new concepts, e.g., the anomalous Floquet states due to hybridization of multiple Floquet sectors with different photon numbers [24–27] and the Floquet fractional Chern insulator states as intrinsic fractionally quantized Hall states under a periodic drive [28], which are attracting a great deal of research interest recently. The circular dichroism of the Floquet states is also studied intensively [29,30].

The Floquet engineering of material topology has been developed further in various directions [31]. On the surfaces of topological insulators, Floquet-Bloch states with ultrafast intraband and interband dynamics are experimentally observed [32,33]. In three-dimensions, Floquet Weyl semimetal states [34,35] as three-dimensional counterparts of the Floquet Chern insulator states have been proposed to emerge in the photodriven three-dimensional Dirac electron systems

[36] and the Mott-insulating magnets on the pyrochlore lattice [37]. Consideration of strong electron correlations is another important direction of the research. The Floquet theory combined with the dynamical mean-field theory (DMFT) named Floquet-DMFT has been developed as a powerful tool to analyze the photodriven phenomena in correlated electron systems [38,39], e.g., manipulation of fermion-fermion interactions [40] and higher-harmonic generations in Mott insulators [41]. In addition, the Floquet engineering extends its scope to the research field of spintronics [42,43]. Analyses based on the Floquet theory have revealed a variety of physical mechanisms of spin-current generation based on spin-wave excitations by application of electromagnetic waves to magnets such as multiferroic materials with magnetoelectric coupling [44]. Spin dynamics toward and in the Floquet states are also active research topics [45,46]. The Floquet engineering continues to attract researchers from the viewpoints of both fundamental science and technical application.

The geometry of lattice structure is a crucial factor for the Floquet engineering [2,47,48]. We argue this aspect by introducing a technical detail of the Floquet theory. The Floquet theory describes nonequilibrium steady states induced by a periodic drive such as light in an extended Hilbert space of states with different photon numbers n , i.e., the original space without the periodic drive ($n = 0$) and duplicated subspaces with $n = \pm 1, \pm 2, \dots$. Because direct analyses of this extended Hilbert space require a huge computational cost, a high-frequency expansion technique is frequently used, in which the duplicated nonzero photon-number subspaces are projected onto the original Hilbert space. In this framework, we often consider the terms up to the first-order of the

expansion with respect to $1/\omega$ for the effective Hamiltonian \hat{H}_{eff} ,

$$\hat{H}_{\text{eff}} = \hat{H}_0 - \sum_{n>0} \frac{[\hat{H}_n, \hat{H}_{-n}]}{n\omega}, \quad (1)$$

$$\hat{H}_n = \frac{1}{T} \int_0^T d\tau \hat{H}(\tau) e^{in\omega\tau}, \quad (2)$$

where $\hat{H}(\tau)$ denotes the original time-dependent Hamiltonian under photoirradiation, and ω and $T = 2\pi/\omega$ denote the frequency and time period of light, respectively. The first term of Eq. (1) describes the time-average of the original Hamiltonian, while the second term describes the projection of one-photon subspaces into the original Hilbert space.

In fact, in the Floquet engineering, the second term plays a substantial role for the emergence of photoinduced topological phases. However, it is known that the first-order terms usually vanish because of the cancellation of contributions from equivalent paths having phases with opposite signs. In fact, we can avoid such cancellations to realize a nonzero contribution from the first-order terms in multipartite lattices, e.g., honeycomb lattices (bipartite), Lieb lattices (bipartite), and Kagome lattices (tripartite). On the contrary, the cancellation cannot be avoided in simple nonmultipartite lattices such as square and triangular lattices even in the presence of extrinsic sublattice degrees of freedom introduced by long-range orders of spins and/or charges. For this reason, lattice electron models on several multipartite lattices such as Kagome lattices, honeycomb lattices, and Lieb lattices have been intensively studied in the research of Floquet engineering, but those on simple square lattices and triangular lattices have not been its major target so far.

Then we encounter the following question: Is it really impossible to conduct the Floquet engineering with electron models on simple nonmultipartite lattices? The answer is no, and the Floquet engineering can indeed be applied to lattice electron models on, e.g., triangular and square lattices. In this paper, we demonstrate that even a simple triangular-lattice system can host rich Floquet topological phases under photoirradiation based on a theoretical study on the photodriven Dirac half-metal state in a Kondo-lattice model with spin-charge coupling. Our Floquet analysis reveals that originally massless half-metallic Dirac electrons become massive under irradiation with circularly polarized light, and, consequently, two kinds of Floquet spin-polarized Chern insulator phases emerge. Importantly, the first-order terms of high-frequency expansion are not relevant to this photoinduced topological phase transition because they completely cancel each other out and vanish on the triangular lattice. Instead, higher-order terms turn out to play a substantial role for emergence of these Floquet topological phases. We also argue that these Floquet Chern insulator phases can be detected and distinguished by a measurement of the Hall conductivity. Our findings are expected to broaden the range of candidate materials for the Floquet engineering.

The rest of this paper is organized as follows. In Sec. II, we describe the extended Ising Kondo-lattice model utilized in this study. In Sec. III, we explain our theoretical framework based on the Floquet theory and the high-frequency expansion. In this section, we also discuss how the first-order terms

of the high-frequency expansion vanish in the nonmultipartite lattice systems. In Sec. IV, we present the results, which include nonequilibrium band structures, nonequilibrium phase diagrams, and the Hall conductivity under irradiation with circularly polarized light. Section V is devoted to summary.

II. MODEL

We start with a triangular Kondo-lattice model which describes the coupling between conduction electrons and localized spins on the triangular lattice [49]. The Hamiltonian is given by

$$\begin{aligned} \mathcal{H}_{\text{IKLM}} = & -t \sum_{(i,j)} \sum_{\sigma=\uparrow,\downarrow} (\hat{c}_{i\sigma}^\dagger \hat{c}_{j\sigma} + \text{H.c.}) \\ & - J_K \sum_i \sum_{\sigma,\sigma'=\uparrow,\downarrow} \hat{c}_{i\sigma}^\dagger \hat{\sigma}_{\sigma\sigma'}^z \hat{c}_{i\sigma'} S_{iz} \\ & + J'_K \sum_i \sum_{j \in \{\text{NN of } i\}} \sum_{\sigma,\sigma'=\uparrow,\downarrow} \hat{c}_{i\sigma}^\dagger \hat{\sigma}_{\sigma\sigma'}^z \hat{c}_{i\sigma'} S_{jz}. \end{aligned} \quad (3)$$

Here $\hat{c}_{i\sigma}^\dagger$ ($\hat{c}_{i\sigma}$) denotes the creation (annihilation) operator of an conduction electron with spin σ ($=\uparrow, \downarrow$) on site i , and $\mathbf{S}_i = (0, 0, S_{iz})$ with $S_{iz} = \pm 1$ is the localized Ising spin on site i . The symbol $\hat{\sigma}^z$ is the Pauli matrix for the spin z component. The first term represents the nearest-neighbor hoppings of conduction electrons, where t is the transfer integral and is used as a unit of energy. The second and third terms describe the intrasite ferromagnetic and intersite antiferromagnetic exchange coupling between the conduction electron spins and the localized Ising spins, respectively, where J_K and J'_K are the coupling constants. We assume a three-sublattice up-up-down ferrimagnetic order of the localized spins [Fig. 1(a)]. This spin structure is known to be realized as the ground state when the electron filling is nearly $1/3$. We assume the limit of strong Ising anisotropy where this magnetic order does not alter under photoirradiation.

In equilibrium, this ferrimagnetic order induces Dirac-cone bands when $(J_K + 3J'_K)/t > 1$, whose Dirac points are located at K-point and $\varepsilon = \pm J_K$. These Dirac-cone bands are perfectly spin polarized. Specifically, the lower-lying Dirac cone around $\varepsilon = -J_K$ is up-spin polarized, whereas the higher-lying Dirac cone around $\varepsilon = +J_K$ is down-spin polarized [Fig. 1(b)]. When the electron filling is $n_e = 1/3$, the lowest two of the six bands are occupied and the lower Dirac point with up-spin polarization is located at the Fermi level. This state is referred to as ‘‘Dirac half metal’’.

In fact, an additional down-spin band overlaps this Dirac point, which inevitably hinders physical responses of the Dirac electrons. The intersite antiferromagnetic Kondo coupling J'_K can remove this down-spin band from the Dirac point through lowering its energy as shown in Fig. 1(c) [49]. This band shift does not change the chemical potential $\mu = -J_K$, which is originally located at the Dirac point of lower-lying Dirac-cone bands. In this situation, we expect physical responses purely from the Dirac electrons, at least, at low temperatures. In the following, we discuss the results obtained for $J_K/t = 2$ and $J'_K/t = 0.05$. Note that this parameter set does satisfy the relation $(J_K + 3J'_K)/t > 1$.

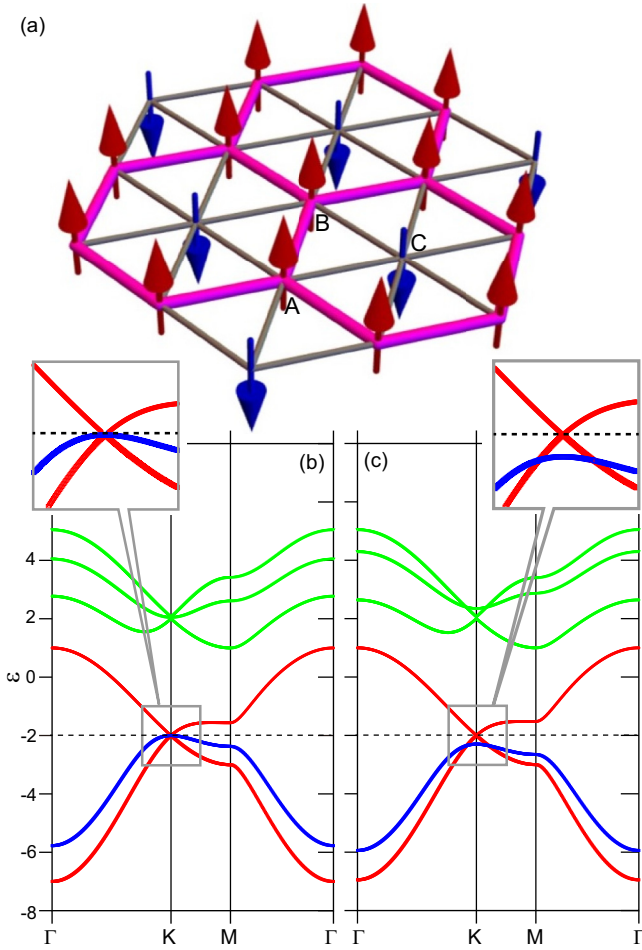


FIG. 1. (a) Up-up-down ferrimagnetic order with three sublattices (A, B, and C) on the triangular lattice. Thick lines indicate a honeycomb network of up-spins. (b) Band dispersion relations for the extended Ising Kondo-lattice model with $J_K/t = 2$ and $J'_K/t = 0$. (c) Those for $J_K/t = 2$ and $J'_K/t = 0.05$. Red and blue colors of the lowest three bands in (b) and (c) indicate the up- and down-spin polarizations, respectively.

When the order of localized spins $\{S_i\}$ is rigid and is never affected by the photoirradiation, the above Kondo-lattice model can be reduced to a tight-binding model with sublattice-dependent on-site potentials as

$$\mathcal{H} = -t \sum_{i \neq j, \sigma} \hat{c}_{i\sigma}^\dagger \hat{c}_{j\sigma} + \sum_{i, \sigma} v_{i, \sigma} \hat{c}_{i\sigma}^\dagger \hat{c}_{i\sigma}, \quad (4)$$

with

$$v_{i, \sigma} = \begin{cases} -J_K \sigma & i \in \text{sublattice A} \\ -J_K \sigma & i \in \text{sublattice B}, \\ (J_K + 6J'_K) \sigma & i \in \text{sublattice C} \end{cases}, \quad (5)$$

where $\sigma = +1$ ($\sigma = -1$) for up (down) spin. This formula is a general form of the Hamiltonian for the noninteracting electron systems with arbitrary on-site potentials.

When this system is irradiated by light, the situation is described by the following Hamiltonian with a time-dependent vector potential $\mathbf{A}(\tau)$,

$$\hat{H}(\tau) = -t \sum_{i \neq j, \sigma} e^{i\mathbf{A}(\tau) \cdot \mathbf{r}_{ij}} \hat{c}_{i\sigma}^\dagger \hat{c}_{j\sigma} + \sum_{i, \sigma} v_{i, \sigma} \hat{c}_{i\sigma}^\dagger \hat{c}_{i\sigma}, \quad (6)$$

where $\mathbf{r}_{ij} \equiv \mathbf{r}_j - \mathbf{r}_i$ denotes the bond vector from site i to site j . The general form of the time-dependent vector potential is given by

$$\mathbf{A}(\tau) = \frac{E_\omega}{\omega} (\mathbf{e}_1 \cos \omega \tau + \mathbf{e}_2 \sin \omega \tau), \quad (7)$$

where \mathbf{e}_1 and \mathbf{e}_2 are arbitrary three-component vectors describing the light polarization. This vector potential generates the light electric field,

$$\mathbf{E}(\tau) = -\frac{\partial \mathbf{A}(\tau)}{\partial \tau} = E_\omega (\mathbf{e}_1 \sin \omega \tau - \mathbf{e}_2 \cos \omega \tau). \quad (8)$$

In this study, we examine the effect of circularly polarized light and thus set $\mathbf{e}_1 = (1, 0, 0)$ and $\mathbf{e}_2 = (0, 1, 0)$.

III. METHODS

We analyze the model in Eq. (6) using the Floquet theory. We also perform real-time simulations based on the time-dependent Schrödinger equation to support the Floquet analysis. In the following, we describe a fundamental formalism of the Floquet theory and its application to noninteracting systems. Then we describe the Keldysh Green's functions to calculate the Hall conductivity in the photoirradiated system in Sec. III B. In Sec. III C, we describe the Brillouin-Wigner expansion as one of the typical high-frequency expansion techniques. In Sec. III D, we discuss how the first-order terms of the Brillouin-Wigner expansion are canceled in the non-multipartite lattice electron systems. In Sec. III E, we explain details of the real-time simulations. We also discuss the unit conversions used in this study in Sec. III F.

A. Floquet theory

The time-dependent Schrödinger equation for noninteracting systems is given by

$$i\hbar \frac{\partial}{\partial \tau} |\psi(\tau)\rangle = \hat{H}(\tau) |\psi(\tau)\rangle, \quad (9)$$

where τ , $\hat{H}(\tau)$ and $|\psi(\tau)\rangle$ denote the time, the noninteracting time-dependent Hamiltonian, and the time-dependent single-particle wave function, respectively. When we consider a time-periodic Hamiltonian $\hat{H}(\tau)$ with a frequency ω , which satisfies $\hat{H}(\tau) = \hat{H}(\tau + T)$ with $T = 2\pi/\omega$, the wave function $|\psi(\tau)\rangle$ is given by

$$|\psi(\tau)\rangle = e^{-i\epsilon\tau/\hbar} |\phi(\tau)\rangle. \quad (10)$$

Here $|\phi(\tau)\rangle$ ($= |\phi(\tau + T)\rangle$) is the time-periodic single-particle state called Floquet state, which has the same time periodicity as that of $\hat{H}(\tau)$, and ϵ denotes the eigenvalue of the

corresponding Floquet state. Equation (10) is the representative formula of the Floquet theorem. Because both $\hat{H}(\tau)$ and $|\phi(\tau)\rangle$ are time periodic, we can expand them by the complex Fourier series as

$$\hat{H}(\tau) = \sum_m e^{-im\omega\tau} \hat{H}_m, \quad (11)$$

$$|\phi(\tau)\rangle = \sum_m e^{-im\omega\tau} |\phi^m\rangle, \quad (12)$$

where the complex Fourier coefficients \hat{H}_m and $|\phi^m\rangle$ are, respectively, given by

$$\hat{H}_m = \frac{1}{T} \int_0^T d\tau \hat{H}(\tau) e^{im\omega\tau}, \quad (13)$$

$$|\phi^m\rangle = \frac{1}{T} \int_0^T d\tau |\phi(\tau)\rangle e^{im\omega\tau}. \quad (14)$$

Here the integer m in \hat{H}_m and $|\phi^m\rangle$ denotes the number of photons.

For $\hat{H}(\tau)$ in Eq. (6), we obtain an explicit formula of the

Fourier coefficient \hat{H}_n as

$$\hat{H}_n = -t \sum_{i \neq j, \sigma} \mathcal{J}_{-n}(\mathcal{A}_{ij}) e^{-in\theta_{ij}} \hat{c}_{i\sigma}^\dagger \hat{c}_{j\sigma} + \delta_{0,n} \sum_{i,\sigma} v_{i\sigma} \hat{c}_{i\sigma}^\dagger \hat{c}_{i\sigma}. \quad (15)$$

We use the following relation in the derivation,

$$\begin{aligned} \frac{1}{T} \int_0^T d\tau \exp\{i\mathcal{A}_{ij} \sin(\omega\tau + \theta_{ij}) + in\omega\tau\} \\ = \mathcal{J}_{-n}(\mathcal{A}_{ij}) e^{-in\theta_{ij}}, \end{aligned} \quad (16)$$

where $\mathcal{J}_n(x)$ is the n -th order Bessel function of the first kind. The quantities \mathcal{A}_{ij} and θ_{ij} are, respectively, given by

$$\mathcal{A}_{ij} = \frac{E_\omega}{\omega} \sqrt{(\mathbf{r}_{ij} \cdot \mathbf{e}_1)^2 + (\mathbf{r}_{ij} \cdot \mathbf{e}_2)^2}, \quad (17)$$

$$\theta_{ij} = \tan^{-1} \left(\frac{\mathbf{r}_{ij} \cdot \mathbf{e}_1}{\mathbf{r}_{ij} \cdot \mathbf{e}_2} \right). \quad (18)$$

Substituting Eqs. (10), (11), and (12) into Eq. (9), we obtain the following eigenvalue equation,

$$(\hat{\mathcal{H}}_F - \omega \hat{\mathcal{M}}_F) |\phi_F\rangle = \varepsilon |\phi_F\rangle, \quad (19)$$

where

$$\hat{\mathcal{H}}_F = \begin{pmatrix} \ddots & & & & & & \ddots \\ \cdots & \hat{H}_{-2,-2} & \hat{H}_{-2,-1} & \hat{H}_{-2,0} & \hat{H}_{-2,+1} & \hat{H}_{-2,+2} & \cdots \\ \cdots & \hat{H}_{-1,-2} & \hat{H}_{-1,-1} & \hat{H}_{-1,0} & \hat{H}_{-1,+1} & \hat{H}_{-1,+2} & \cdots \\ \cdots & \hat{H}_{0,-2} & \hat{H}_{0,-1} & \hat{H}_{0,0} & \hat{H}_{0,+1} & \hat{H}_{0,+2} & \cdots \\ \cdots & \hat{H}_{+1,-2} & \hat{H}_{+1,-1} & \hat{H}_{+1,0} & \hat{H}_{+1,+1} & \hat{H}_{+1,+2} & \cdots \\ \cdots & \hat{H}_{+2,-2} & \hat{H}_{+2,-1} & \hat{H}_{+2,0} & \hat{H}_{+2,+1} & \hat{H}_{+2,+2} & \cdots \\ \ddots & & & & & & \ddots \end{pmatrix}, \quad (20)$$

$$\hat{\mathcal{M}}_F = \begin{pmatrix} \ddots & & & & & & \ddots \\ \cdots & -2\hat{I}_r & \hat{O}_r & \hat{O}_r & \hat{O}_r & \hat{O}_r & \cdots \\ \cdots & \hat{O}_r & -\hat{I}_r & \hat{O}_r & \hat{O}_r & \hat{O}_r & \cdots \\ \cdots & \hat{O}_r & \hat{O}_r & \hat{O}_r & \hat{O}_r & \hat{O}_r & \cdots \\ \cdots & \hat{O}_r & \hat{O}_r & \hat{O}_r & +\hat{I}_r & \hat{O}_r & \cdots \\ \cdots & \hat{O}_r & \hat{O}_r & \hat{O}_r & \hat{O}_r & +2\hat{I}_r & \cdots \\ \ddots & & & & & & \ddots \end{pmatrix}. \quad (21)$$

In the real-space representation, the matrix \mathcal{H}_F is composed of $2N \times 2N$ -dimensional block matrices $\hat{H}_{n,m} \equiv \hat{H}_{n-m}$. The matrices \hat{I}_r and \hat{O}_r are $2N \times 2N$ -dimensional identity matrix and zero matrix, respectively. The Floquet-state vector $|\phi_F\rangle$ in the real-space representation is defined as

$$|\phi_F\rangle = {}^t (\cdots, \{\phi_{i\sigma}^{-2}\}, \{\phi_{i\sigma}^{-1}\}, \{\phi_{i\sigma}^0\}, \{\phi_{i\sigma}^1\}, \{\phi_{i\sigma}^2\}, \cdots), \quad (22)$$

where $\{\phi_{i\sigma}^n\}$ is a set of $2N$ components $\phi_{i\sigma}^n$ of the n -photon Floquet-state vector $|\phi^n\rangle$ with $i = 1, 2, \dots, N$ and $\sigma = \pm 1$. In this way, the time-dependent Schrödinger equation in

Eq. (9) with a time-periodic Hamiltonian $\hat{H}(\tau)$ is mapped onto the time-independent eigenvalue problem given by Eq. (19).

Using the Fourier transforms,

$$\hat{c}_{i\sigma}^\dagger = \frac{1}{\sqrt{N}} \sum_k \hat{c}_k^\dagger e^{-ik \cdot \mathbf{r}_i}, \quad \hat{c}_{i\sigma} = \frac{1}{\sqrt{N}} \sum_k \hat{c}_k e^{ik \cdot \mathbf{r}_i}, \quad (23)$$

we rewrite Eq. (19) in the momentum-space representation as

$$(\hat{\mathcal{H}}_F(\mathbf{k}) - \omega \hat{\mathcal{M}}_F) |\phi_F(\mathbf{k})\rangle = \varepsilon_{\mathbf{k}} |\phi_F(\mathbf{k})\rangle, \quad (24)$$

where

$$\hat{\mathcal{H}}_F(\mathbf{k}) = \begin{pmatrix} \ddots & \vdots & \vdots & \vdots & \vdots & \vdots & \ddots \\ \cdots & \hat{H}_{-2,-2}(\mathbf{k}) & \hat{H}_{-2,-1}(\mathbf{k}) & \hat{H}_{-2,0}(\mathbf{k}) & \hat{H}_{-2,+1}(\mathbf{k}) & \hat{H}_{-2,+2}(\mathbf{k}) & \cdots \\ \cdots & \hat{H}_{-1,-2}(\mathbf{k}) & \hat{H}_{-1,-1}(\mathbf{k}) & \hat{H}_{-1,0}(\mathbf{k}) & \hat{H}_{-1,+1}(\mathbf{k}) & \hat{H}_{-1,+2}(\mathbf{k}) & \cdots \\ \cdots & \hat{H}_{0,-2}(\mathbf{k}) & \hat{H}_{0,-1}(\mathbf{k}) & \hat{H}_{0,0}(\mathbf{k}) & \hat{H}_{0,+1}(\mathbf{k}) & \hat{H}_{0,+2}(\mathbf{k}) & \cdots \\ \cdots & \hat{H}_{+1,-2}(\mathbf{k}) & \hat{H}_{+1,-1}(\mathbf{k}) & \hat{H}_{+1,0}(\mathbf{k}) & \hat{H}_{+1,+1}(\mathbf{k}) & \hat{H}_{+1,+2}(\mathbf{k}) & \cdots \\ \cdots & \hat{H}_{+2,-2}(\mathbf{k}) & \hat{H}_{+2,-1}(\mathbf{k}) & \hat{H}_{+2,0}(\mathbf{k}) & \hat{H}_{+2,+1}(\mathbf{k}) & \hat{H}_{+2,+2}(\mathbf{k}) & \cdots \\ \ddots & \vdots & \vdots & \vdots & \vdots & \vdots & \ddots \end{pmatrix}, \quad (25)$$

$$\hat{\mathcal{M}}_m = \begin{pmatrix} \ddots & \vdots & \vdots & \vdots & \vdots & \vdots & \ddots \\ \cdots & -2\hat{I}_m & \hat{O}_m & \hat{O}_m & \hat{O}_m & \hat{O}_m & \cdots \\ \cdots & \hat{O}_m & -\hat{I}_m & \hat{O}_m & \hat{O}_m & \hat{O}_m & \cdots \\ \cdots & \hat{O}_m & \hat{O}_m & \hat{O}_m & \hat{O}_m & \hat{O}_m & \cdots \\ \cdots & \hat{O}_m & \hat{O}_m & \hat{O}_m & +\hat{I}_m & \hat{O}_m & \cdots \\ \cdots & \hat{O}_m & \hat{O}_m & \hat{O}_m & \hat{O}_m & +2\hat{I}_m & \cdots \\ \ddots & \vdots & \vdots & \vdots & \vdots & \vdots & \ddots \end{pmatrix}. \quad (26)$$

The matrix $\hat{\mathcal{H}}_F(\mathbf{k})$ is composed of 6×6 -dimensional block matrices $\hat{H}_{n,m}(\mathbf{k}) \equiv \hat{H}_{n-m}(\mathbf{k})$. The matrices \hat{I}_m and \hat{O}_m are 6×6 -dimensional identity matrix and zero matrix, respectively. The Floquet-state vector $|\phi_F(\mathbf{k})\rangle$ in the momentum space is defined as

$$|\phi_F(\mathbf{k})\rangle = {}^t (\cdots, \{\phi_\nu^{-2}(\mathbf{k})\}, \{\phi_\nu^{-1}(\mathbf{k})\}, \{\phi_\nu^0(\mathbf{k})\}, \{\phi_\nu^1(\mathbf{k})\}, \\ \times \{\phi_\nu^2(\mathbf{k})\}, \cdots), \quad (27)$$

where ν is the band index. The present system has six bands for each photon-number subspace (i.e., $\nu = 1, 2, \dots, 6$) because of the three sublattices and the spins $\sigma = \pm 1$. Here $\{\phi_\nu^n(\mathbf{k})\}$ is a set of six components $\phi_\nu^n(\mathbf{k})$ of the n -photon Floquet-state vector $|\phi^n(\mathbf{k})\rangle$ at momentum \mathbf{k} . For practical treatment of Eq. (24), we restrict the number of photons to $|n| \leq n_{\max}$ with $n_{\max} = 16$ throughout the present study. After

this truncation, we obtain the band dispersion relations $\varepsilon_\nu^n(\mathbf{k})$ and the eigenstates $|\phi_\nu^n(\mathbf{k})\rangle$ by diagonalizing the truncated Floquet Hamiltonian $\hat{\mathcal{H}}_F(\mathbf{k}) - \omega \hat{\mathcal{M}}_m$.

B. Keldysh Green's function formalism

The Chern number of the ν th band in the Floquet state and the Hall conductivity under photoirradiation are respectively given by [1,31,50]

$$N_{\text{Ch}}^\nu = \frac{1}{2\pi} \int_{\text{BZ}} d\mathbf{k} \Omega_z^\nu(\mathbf{k}), \quad (28)$$

$$\sigma_{xy} = \frac{e^2}{h} \frac{1}{2\pi} \sum_\nu \int_{\text{BZ}} d\mathbf{k} n_\nu(\mathbf{k}) \Omega_z^\nu(\mathbf{k}). \quad (29)$$

The Berry curvature $\Omega_z^\nu(\mathbf{k})$ is given by

$$\Omega_z^\nu(\mathbf{k}) = i \sum_{(m,\mu) \neq (n,\nu)} \frac{\langle \phi_\nu^n(\mathbf{k}) | \partial_{k_x} \hat{\mathcal{H}}_F(\mathbf{k}) | \phi_\mu^m(\mathbf{k}) \rangle \langle \phi_\mu^m(\mathbf{k}) | \partial_{k_y} \hat{\mathcal{H}}_F(\mathbf{k}) | \phi_\nu^n(\mathbf{k}) \rangle}{[\varepsilon_\nu^n(\mathbf{k}) - \varepsilon_\mu^m(\mathbf{k})]^2}. \quad (30)$$

The nonequilibrium electron distribution function $n_\nu(\mathbf{k})$ represents the expectation value of electron occupation of the state with a momentum \mathbf{k} and the band index ν . For the off-resonant condition that all the Floquet sidebands with nonzero photon number $n \neq 0$ do not overlap the original band set with $n = 0$, we can simply approximate $n_\nu(\mathbf{k}) \sim f(\varepsilon_\nu^0(\mathbf{k}))$ where $f(\varepsilon)$ is the Fermi distribution function in equilibrium. On the contrary, for the on-resonant condition that some of the Floquet sidebands overlap the original bands, this approximation no longer holds. Therefore, we need to calculate $n_\nu(\mathbf{k})$ for evaluating the Hall conductivity.

We utilize Keldysh Green's function method [39,51] to calculate $n_\nu(\mathbf{k})$. The Dyson equation for the Green's function

matrix is given by

$$\begin{pmatrix} \hat{G}^R(\mathbf{k}, \varepsilon) & \hat{G}^K(\mathbf{k}, \varepsilon) \\ 0 & \hat{G}^A(\mathbf{k}, \varepsilon) \end{pmatrix}^{-1} \\ = \begin{pmatrix} [\hat{G}^{R0}(\mathbf{k}, \varepsilon)]^{-1} & [\hat{G}^{K0}(\mathbf{k}, \varepsilon)]^{-1} \\ 0 & [\hat{G}^{A0}(\mathbf{k}, \varepsilon)]^{-1} \end{pmatrix} - \begin{pmatrix} \hat{\Sigma}^R & \hat{\Sigma}^K(\varepsilon) \\ 0 & \hat{\Sigma}^A \end{pmatrix}, \quad (31)$$

where \hat{G}^R , \hat{G}^A , and \hat{G}^K ($\hat{\Sigma}^R$, $\hat{\Sigma}^A$, and $\hat{\Sigma}^K$) are the retarded, advanced, and Keldysh Green's functions (self-energies) for the Floquet states, respectively. Matrix elements of the

noninteracting Green's functions for the Floquet states and the self-energies are respectively given by

$$[\hat{G}^{\text{R0}}(\mathbf{k}, \varepsilon)]_{nv, m\mu}^{-1} = \varepsilon \delta_{nm} \delta_{v\mu} - [\mathcal{H}_{\text{F}}(\mathbf{k}) - \omega \mathcal{M}_{\text{m}}]_{nv, m\mu}, \quad (32)$$

$$[\hat{G}^{\text{R0}}(\mathbf{k}, \varepsilon)]_{nv, m\mu}^{-1} = \varepsilon \delta_{nm} \delta_{v\mu} - [\mathcal{H}_{\text{F}}(\mathbf{k}) - \omega \mathcal{M}_{\text{m}}]_{nv, m\mu}, \quad (33)$$

$$[\hat{\Sigma}^{\text{R}}]_{nv, m\mu} = -i\Gamma \delta_{nm} \delta_{v\mu}, \quad (34)$$

$$[\hat{\Sigma}^{\text{A}}]_{nv, m\mu} = i\Gamma \delta_{nm} \delta_{v\mu}, \quad (35)$$

$$[\hat{\Sigma}^{\text{K}}(\varepsilon)]_{nv, m\mu} = -2i\Gamma \tanh\left[\frac{\varepsilon - \mu + m\omega}{2k_{\text{B}}T_{\text{hr}}}\right] \delta_{nm} \delta_{v\mu}, \quad (36)$$

where Γ represents the strength of dissipation due to the coupling to a heat reservoir at temperature T_{hr} . We set $\Gamma/t = 0.1$ in this study. Then, the lesser Green's function $\hat{G}^<$ is given by

$$\hat{G}^<(\mathbf{k}, \varepsilon) = \hat{G}^{\text{R}}(\mathbf{k}, \varepsilon) \hat{\Sigma}^<(\varepsilon) \hat{G}^{\text{A}}(\mathbf{k}, \varepsilon), \quad (37)$$

where the lesser self-energy $\hat{\Sigma}^<$ is given by,

$$\hat{\Sigma}^<(\varepsilon) = \frac{\hat{\Sigma}^{\text{A}} + \hat{\Sigma}^{\text{K}}(\varepsilon) - \hat{\Sigma}^{\text{R}}}{2}. \quad (38)$$

Finally, the nonequilibrium electron distribution $n_v(\mathbf{k})$ with momentum \mathbf{k} and band index v is given by

$$n_v(\mathbf{k}) = \frac{\langle \phi_v^0(\mathbf{k}) | \hat{N}_k(\varepsilon_v^0(\mathbf{k})) | \phi_v^0(\mathbf{k}) \rangle}{\langle \phi_v^0(\mathbf{k}) | \hat{A}_k(\varepsilon_v^0(\mathbf{k})) | \phi_v^0(\mathbf{k}) \rangle}, \quad (39)$$

where the operators \hat{A} and \hat{N} are respectively given by

$$\hat{A}_k(\varepsilon) = \frac{i}{2\pi} (\hat{G}^{\text{R}}(\mathbf{k}, \varepsilon) - \hat{G}^{\text{A}}(\mathbf{k}, \varepsilon)), \quad (40)$$

$$\hat{N}_k(\varepsilon) = -\frac{i}{2\pi} \hat{G}^<(\mathbf{k}, \varepsilon). \quad (41)$$

In this study, we use 144×144 \mathbf{k} -points for numerical calculations. The chemical potential μ is determined by using the bisection method to preserve the total electron number n_e . We iterate the Keldysh Green's function calculation to tune the chemical potential until the value of n_e becomes very close to the target value. In the following, we keep $n_e = 0.34$ with negligibly small errors less than 10^{-8} .

C. Brillouin-Wigner expansion

To study the effect of lattice geometry on the electron states in the photoirradiated system, we adopt the Brillouin-Wigner expansion [47], which is one of the typical high-frequency expansion techniques [52–55]. The high-frequency expansion is accurate in the limit of $\omega \rightarrow \infty$ where $2\pi/\omega$ is a time periodicity of the Hamiltonian. The expansion gives an effective Hamiltonian \hat{H}_{BW} called Brillouin-Wigner Hamiltonian, which describes the electron states under photoirradiation and is obtained by an appropriate projection of nonzero photon-number subspaces of $\mathcal{H}_{\text{F}} - \omega \mathcal{M}_{\text{r}}$ to the original Hilbert space with zero photon number. The Brillouin-Wigner Hamiltonian is given by

$$\hat{H}_{\text{BW}} = \sum_{n=0,1,2,\dots} \hat{H}_{\text{BW}}^{(n)}, \quad (42)$$

with

$$\hat{H}_{\text{BW}}^{(0)} = \hat{H}_{0,0}, \quad (43)$$

$$\hat{H}_{\text{BW}}^{(1)} = \sum_{n \neq 0} \frac{\hat{H}_{0,n} \hat{H}_{n,0}}{n\omega} = -\sum_{n > 0} \frac{[\hat{H}_n, \hat{H}_{-n}]}{n\omega}, \quad (44)$$

$$\hat{H}_{\text{BW}}^{(2)} = \sum_{n_1, n_2 \neq 0} \frac{\hat{H}_{0,n_1} \hat{H}_{n_1, n_2} \hat{H}_{n_2, 0}}{n_1 n_2 \omega^2} - \sum_{n \neq 0} \frac{\hat{H}_{0,n} \hat{H}_{n,0} \hat{H}_{0,0}}{n^2 \omega^2}, \quad (45)$$

$$\begin{aligned} \hat{H}_{\text{BW}}^{(3)} = & \sum_{n_1, n_2, n_3 \neq 0} \frac{\hat{H}_{0,n_1} \hat{H}_{n_1, n_2} \hat{H}_{n_2, n_3} \hat{H}_{n_3, 0}}{n_1 n_2 n_3 \omega^3} \\ & + \sum_{n \neq 0} \frac{\hat{H}_{0,n} \hat{H}_{n,0} \hat{H}_{0,0} \hat{H}_{0,0}}{n^3 \omega^3} \\ & - \sum_{n_1, n_2 \neq 0} \frac{\hat{H}_{0,n_1} \hat{H}_{n_1,0} \hat{H}_{0,n_2} \hat{H}_{n_2,0}}{n_1^2 n_2 \omega^3} \\ & - \sum_{n_1, n_2 \neq 0} \frac{\hat{H}_{0,n_1} \hat{H}_{n_1, n_2} \hat{H}_{n_2,0} \hat{H}_{0,0}}{n_1 n_2 \omega^3} \left(\frac{1}{n_1} + \frac{1}{n_2} \right). \end{aligned} \quad (46)$$

Note that all the n -th order terms are the order of $(1/\omega)^n$. We neglect emergent many-body terms in $\hat{H}_{\text{BW}}^{(2)}$ and $\hat{H}_{\text{BW}}^{(3)}$ which have no influence on the Floquet single-particle states in the noninteracting systems [47].

D. Cancellation of the first-order terms

We discuss how the first-order terms of the Brillouin-Wigner expansion in the nonmultipartite lattice electron systems vanish through mutual cancellation. The numerator of Eq. (44) can be calculated by substituting Eq. (15) into Eq. (44). The explicit calculations are done for $n > 0$ as

$$\begin{aligned} [\hat{H}_n, \hat{H}_{-n}] = & \sum_{i,j} \sum_{k,l} t_{ij} t_{kl} \mathcal{J}_{-n}(\mathcal{A}_{ij}) \mathcal{J}_n(\mathcal{A}_{kl}) e^{-in(\theta_{ij} - \theta_{kl})} \\ & \times [\hat{c}_i^\dagger \hat{c}_j, \hat{c}_k^\dagger \hat{c}_l] \\ = & 2i(-1)^{n+1} \sum_{i,j} \sum_k t_{ik} t_{kj} \mathcal{J}_n(\mathcal{A}_{ik}) \mathcal{J}_n(\mathcal{A}_{kj}) \\ & \times \sin\{n(\theta_{ik} - \theta_{kj})\} \hat{c}_i^\dagger \hat{c}_j. \end{aligned} \quad (47)$$

Here we omit the spin indices for simplicity, but the generality of the argument is not compromised by consideration of the spin degrees of freedom. These terms describe three-site hoppings of conduction electrons from site i to site j via site k ($i \rightarrow k \rightarrow j$) mediated by two nearest neighbor hoppings t . Importantly, in the two- and three-dimensional lattices without sublattice degrees of freedom, every three-site hopping path ($i \rightarrow k_1 \rightarrow j$) has its counterpart ($i \rightarrow k_2 \rightarrow j$), which satisfies the following relations,

$$t_{ik_1} t_{k_1 j} \mathcal{J}_n(\mathcal{A}_{ik_1}) \mathcal{J}_n(\mathcal{A}_{k_1 j}) = t_{ik_2} t_{k_2 j} \mathcal{J}_n(\mathcal{A}_{ik_2}) \mathcal{J}_n(\mathcal{A}_{k_2 j}), \quad (48)$$

$$\theta_{ik_1} - \theta_{k_1 j} = -(\theta_{ik_2} - \theta_{k_2 j}). \quad (49)$$

These relations indicate that the summation over k in the rightmost side of Eq. (47) leads to a perfect cancellation of the first-order terms. Examples of the pairs of three-site hopping paths ($i \rightarrow k_1 \rightarrow j$) and ($i \rightarrow k_2 \rightarrow j$) on the triangular

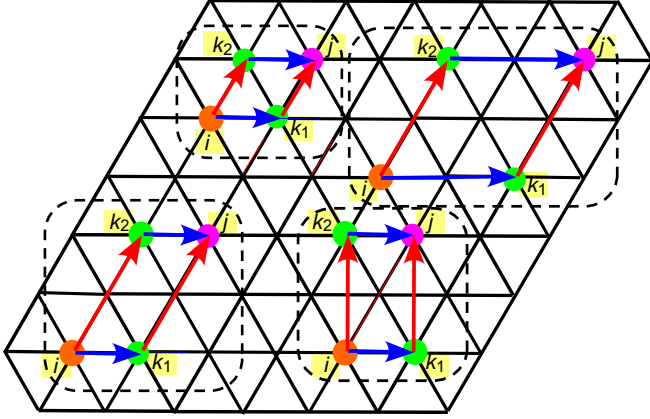


FIG. 2. Examples of pairs of three-site hopping paths ($i \rightarrow k_1 \rightarrow j$) and ($i \rightarrow k_2 \rightarrow j$) whose contributions to indirect hoppings from site i to site j cancel each other.

lattice are shown in Fig. 2, whose contributions to indirect hoppings from site i to site j cancel each other. In contrast, the contributions from the first-order terms survive in the multipartite lattices, such as honeycomb lattices, Lieb lattices, and Kagome lattices. This situation is hardly changed even if further neighbor transfer integrals are considered for these lattices.

E. Real-time simulations based on the time-dependent Schrödinger equation

In addition to the Floquet analysis, we also perform numerical simulations for real-time electron dynamics under photoirradiation based on the time-dependent Schrödinger equation. The time-dependent Schrödinger equation in Eq. (9) can be formally solved in the form,

$$|\psi_v(\mathbf{k}, \tau + \Delta\tau)\rangle = \mathcal{T} \exp \left[-i \int_{\tau}^{\tau + \Delta\tau} d\tau' \mathcal{H}_k(\tau') \right] |\psi_v(\mathbf{k}, \tau)\rangle, \quad (50)$$

where $|\psi_v(\mathbf{k}, \tau)\rangle$ is the single-particle state of v th band with momentum \mathbf{k} and time τ , $\mathcal{H}_k(\tau')$ denotes the \mathbf{k} -resolved Hamiltonian with time τ' , and \mathcal{T} is the time-ordering operator. The single-particle excitation spectrum is given by [56,57]

$$A(\mathbf{k}, \varepsilon) = \text{Im} \sum_{i,\sigma} \int d\tau_1 d\tau_2 s_{\text{pr}}(\tau_1; \tau_{\text{pr}}, \sigma_{\text{pr}}) s_{\text{pr}}(\tau_2; \tau_{\text{pr}}, \sigma_{\text{pr}}) \times e^{i\varepsilon(\tau_1 - \tau_2)} [G_{k,ii\sigma}^<(\tau_1, \tau_2) - G_{k,ii\sigma}^>(\tau_1, \tau_2)], \quad (51)$$

with

$$G_{k,ij\sigma\sigma'}^<(\tau_1, \tau_2) = i \langle \hat{c}_{k,j\sigma'}^\dagger(\tau_2) \hat{c}_{k,i\sigma}(\tau_1) \rangle, \quad (52)$$

$$G_{k,ij\sigma\sigma'}^>(\tau_1, \tau_2) = -i \langle \hat{c}_{k,i\sigma}(\tau_1) \hat{c}_{k,j\sigma'}^\dagger(\tau_2) \rangle. \quad (53)$$

The lesser and greater Green's functions $G_{k,ii\sigma}^<(\tau_1, \tau_2)$ and $G_{k,ii\sigma}^>(\tau_1, \tau_2)$ correspond to occupied and unoccupied states of the i th site with momentum \mathbf{k} and spin σ ($=\uparrow, \downarrow$), respectively. $s_{\text{pr}}(t; \tau_{\text{pr}}, \sigma_{\text{pr}})$ denotes the normalized Gaussian wave

TABLE I. Unit conversions when the transfer integral is $t = 0.1$ eV and the lattice constant is $a = 5$ Å. The variables with (without) tilde denote dimensionful (dimensionless) quantities.

Quantity	Dimensionless quantity	Corresponding values
Frequency	$\omega = \hbar\tilde{\omega}/t = 1$	$\tilde{\omega} = 24.2$ THz
Light electric field	$E_\omega = ea\tilde{E}_\omega/t = 1$	$\tilde{E}_\omega = 2$ MV cm ⁻¹
Time	$\tau = \tilde{\tau}t/\hbar = 1$	$\tilde{\tau} = 6.6$ fs
Temperature	$T_{\text{hr}} = k_B\tilde{T}_{\text{hr}}/t = 1$	$\tilde{T}_{\text{hr}} = 1163$ K

packet of the probe pulse given in the form,

$$s_{\text{pr}}(\tau; \tau_{\text{pr}}, \sigma_{\text{pr}}) = \frac{1}{\sqrt{2\pi}\sigma_{\text{pr}}} \exp \left[-\frac{(\tau - \tau_{\text{pr}})^2}{2\sigma_{\text{pr}}^2} \right], \quad (54)$$

where τ_{pr} and σ_{pr} are the pulse center and the pulse width, respectively. The effect of pump pulse, which is treated as a time-periodic external field in the framework of the Floquet theory, is also taken into account by means of the Peierls substitution $\mathbf{k} \rightarrow \mathbf{k} + \mathbf{A}(\tau)$. The vector potential that mimics a circularly polarized pump pulse with the Gaussian envelope is given by

$$\mathbf{A}_{\text{pu}}(\tau) = \frac{E_\omega}{\omega} \exp \left[-\frac{(\tau - \tau_{\text{pu}})^2}{2\sigma_{\text{pu}}^2} \right] (\mathbf{e}_1 \cos \omega\tau + \mathbf{e}_2 \sin \omega\tau), \quad (55)$$

with maximum electric field strength of E_ω and the frequency of ω . Here τ_{pu} and σ_{pu} are the pulse center and the pulse width, respectively. We set $(\tau_{\text{pu}}, \tau_{\text{pr}}, \sigma_{\text{pu}}, \sigma_{\text{pr}}) = (500T, 500T, 76T, 25T)$ in this work. We solve the time-dependent Schrödinger equation in Eq. (50) in the time window of $t \in [0, 1000T]$ with the time step of $\Delta\tau = T/800$ where $T = 2\pi/\omega$. The initial states $\{|\psi_v(\mathbf{k}, 0)\rangle\}$ are set to be the eigenstates of $\mathcal{H}_{\text{IKLM}}(\mathbf{k})$ in equilibrium where $\mathbf{A}(\tau) = 0$. The exponential function in Eq. (50) is expanded up to the 20th order.

IV. RESULTS

A. Phase diagram

We first study nonequilibrium steady states of electrons under irradiation with circularly polarized light by using the truncated Floquet Hamiltonian $\mathcal{H}_F(\mathbf{k}) - \omega\mathcal{M}_m$. To construct a phase diagram, we calculate $E_\omega\text{-}\omega$ profiles of several physical quantities, i.e., Chern number of the third band N_{Ch}^3 , indirect band gap Δ_{23} , and direct band gap $\tilde{\Delta}_{23}$ by diagonalizing the truncated Floquet Hamiltonian. The obtained profiles are shown in Figs. 3(b)–3(d), respectively. Note that we adopt the natural units $e = \hbar = c = 1$ for the following calculations. Table I summarizes the unit conversions when we assume $t = 0.1$ eV and $a = 5$ Å for the transfer integral and the lattice constant, respectively.

The original six bands are divided into two band sets with three bands each separated by the exchange gap. Importantly, sums of the Chern numbers N_{Ch}^ν over the three bands within a band set become zero, that is, $\sum_{\nu=1}^3 N_{\text{Ch}}^\nu = 0$ and $\sum_{\nu=4}^6 N_{\text{Ch}}^\nu = 0$. Accordingly, when the electron filling is nearly 1/3 with only the lowest two of six bands originally filled with

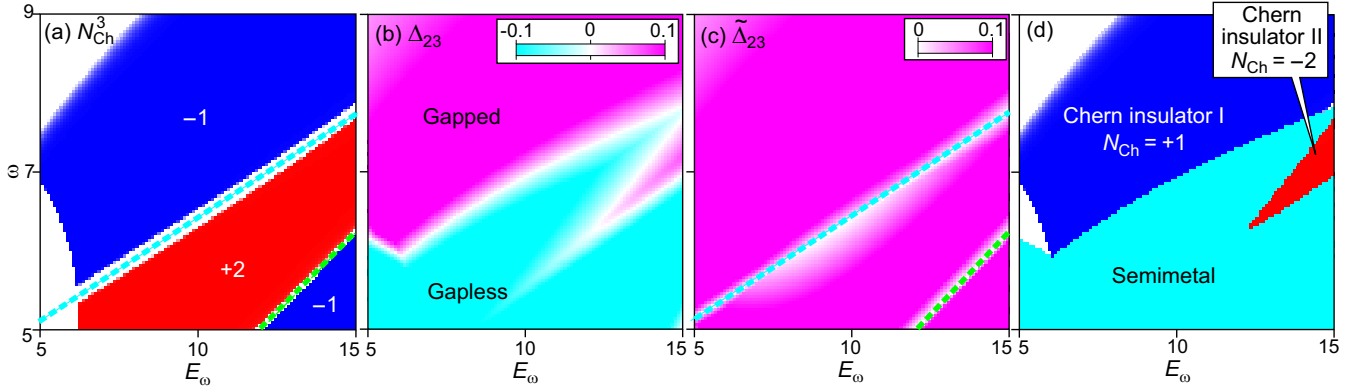


FIG. 3. (a)–(c) E_ω - ω profiles of (a) the Chern number of the third band N_{Ch}^3 , (b) the indirect band gap Δ_{23} , and (c) the direct band gap $\tilde{\Delta}_{23}$ calculated by diagonalizing the truncated Floquet Hamiltonian $\mathcal{H}_F(\mathbf{k}) - \omega\mathcal{M}_m$. (d) Nonequilibrium phase diagram in the plane of light amplitude E_ω and frequency ω under irradiation with circularly polarized light, which is constructed from the E_ω - ω profiles of the physical quantities in (a)–(c).

electrons, the Chern number of the system $N_{\text{Ch}} = \sum_{v \in \text{filled}} N_{\text{Ch}}^v$ is related with N_{Ch}^3 as $N_{\text{Ch}} = -N_{\text{Ch}}^3$. In Fig. 3(a), we find two regions with $N_{\text{Ch}}^3 = -1$ ($N_{\text{Ch}} = +1$) separated by a region with $N_{\text{Ch}}^3 = +2$ ($N_{\text{Ch}} = -2$).

The $N_{\text{Ch}}^3 = -1$ phase in the high-frequency regime is caused by a gap opening at the K point as discussed in Sec. IV B. As the system approaches from the high-frequency $N_{\text{Ch}}^3 = -1$ phase to the $N_{\text{Ch}}^3 = +2$ phase, the band gap at the M point gradually closes and completely vanishes at the boundary between these two phases. Subsequently, the gap reopens at the M point as the system enters the $N_{\text{Ch}}^3 = +2$ phase as described in Sec. IV C. On the contrary, the boundary between the $N_{\text{Ch}}^3 = +2$ phase and the low-frequency $N_{\text{Ch}}^3 = -1$ phase corresponds to the point at which the flat band appears with vanishing bandwidth due to the dynamical localization. According to the Floquet theory, the transfer integrals under a periodic drive are renormalized by a factor of the Bessel function $\mathcal{J}_0(E_\omega/\omega)$, and the factor becomes zero at this phase boundary. We also note that the Chern number is ill-defined in the white regions because the band gap is too small.

The E_ω - ω profiles of two types of band gaps (indirect and direct gaps) between the second and the third bands are shown in Figs. 3(b) and 3(c). The indirect and direct band gaps $\Delta_{\mu\nu}$ and $\tilde{\Delta}_{\mu\nu}$ between the μ th and ν th bands are defined by

$$\Delta_{\mu\nu} = \min_{\mathbf{k} \in \text{BZ}} [\varepsilon_\nu^0(\mathbf{k})] - \max_{\mathbf{k} \in \text{BZ}} [\varepsilon_\mu^0(\mathbf{k})], \quad (56)$$

$$\tilde{\Delta}_{\mu\nu} = \min_{\mathbf{k} \in \text{BZ}} [\varepsilon_\nu^0(\mathbf{k}) - \varepsilon_\mu^0(\mathbf{k})]. \quad (57)$$

According to Δ_{23} , we judge whether the system is gapped/insulating ($\Delta_{23} > 0$) or gapless/metallic ($\Delta_{23} < 0$). On the other hand, we capture the closing of direct band gap according to $\tilde{\Delta}_{23}$, which becomes zero on the dashed lines in Fig. 3(c). These two lines correspond to the two phase boundaries in Fig. 3(a), i.e., a phase boundary at which the gap closes at M points and another phase boundary at which the doubly degenerate up-spin-polarized bands appear.

The E_ω - ω profiles of the physical quantities in Figs. 3(a)–3(c) are summarized into a phase diagram in Fig. 3(d). We assign the region with $\Delta_{23} < 0$ to a semimetal phase irrespective of the value of N_{Ch} . On the contrary, we assign the regions

with $\Delta_{23} > 0$ and nonzero quantized N_{Ch} to a Chern insulator phase. We have two types of Chern insulator phases, i.e., the phase I with $N_{\text{Ch}} = +1$ and the phase II with $N_{\text{Ch}} = -2$.

B. Single-particle spectra

To understand how these Floquet Chern insulator phases appear, we investigate the Floquet band structures under photoirradiation. Figures 4(a)–4(d) show the single-particle spectra $A(\mathbf{q}, \varepsilon)$ calculated by real-time simulations of the time-dependent Schrödinger equation (color) and the Floquet band structures calculated by diagonalization of the truncated Floquet Hamiltonian $\mathcal{H}_F(\mathbf{k}) - \omega\mathcal{M}_m$ (green solid lines) for various values of E_ω when ω is fixed at 8. The value of E_ω is increased as indicated by a horizontal arrow in Fig. 4(e).

Figure 4(a) indicates that the Dirac point located at K point is almost gapless when the light amplitude is as small as $E_\omega = 2$. The Dirac gap is gradually opened with increasing E_ω , and eventually the Dirac point is apparently gapped when the light amplitude is as large as $E_\omega = 12$ as seen in Fig. 4(d). In the presence of the gap, the two lowest bands acquire a nonzero Chern number of $N_{\text{Ch}} = 1$ in total. Note that the band gap between the second and third bands on the M point is always opened irrespective of the value of E_ω .

In the Floquet band structures, the band set, which almost perfectly overlaps the single-particle spectrum, corresponds to the electron states with zero-photon absorption. In addition to this original band set, the equivalent band sets repeatedly appear with an energy interval of ω , which correspond to the n -photon absorbed (emitted) electron states and are referred to as the Floquet sidebands. When the light amplitude is as small as $E_\omega = 2$ in Fig. 4(a), we find that the original band set and the Floquet sideband sets located right above and below it partially overlap, because the light frequency of $\omega = 8$ is smaller than the bandwidth of $W \sim 12$ (i.e., $\omega < W$). This situation is referred to as the on-resonant case.

The overlap of band sets occurs also when $E_\omega = 4$ and $E_\omega = 8$. In this on-resonant case, band-anticrossing occurs at specific points indicated by solid circles. Interestingly, the spectral weight $A(\mathbf{q}, \varepsilon)$ is extended to the sidebands at the band-anticrossing point, which indicates that the Floquet

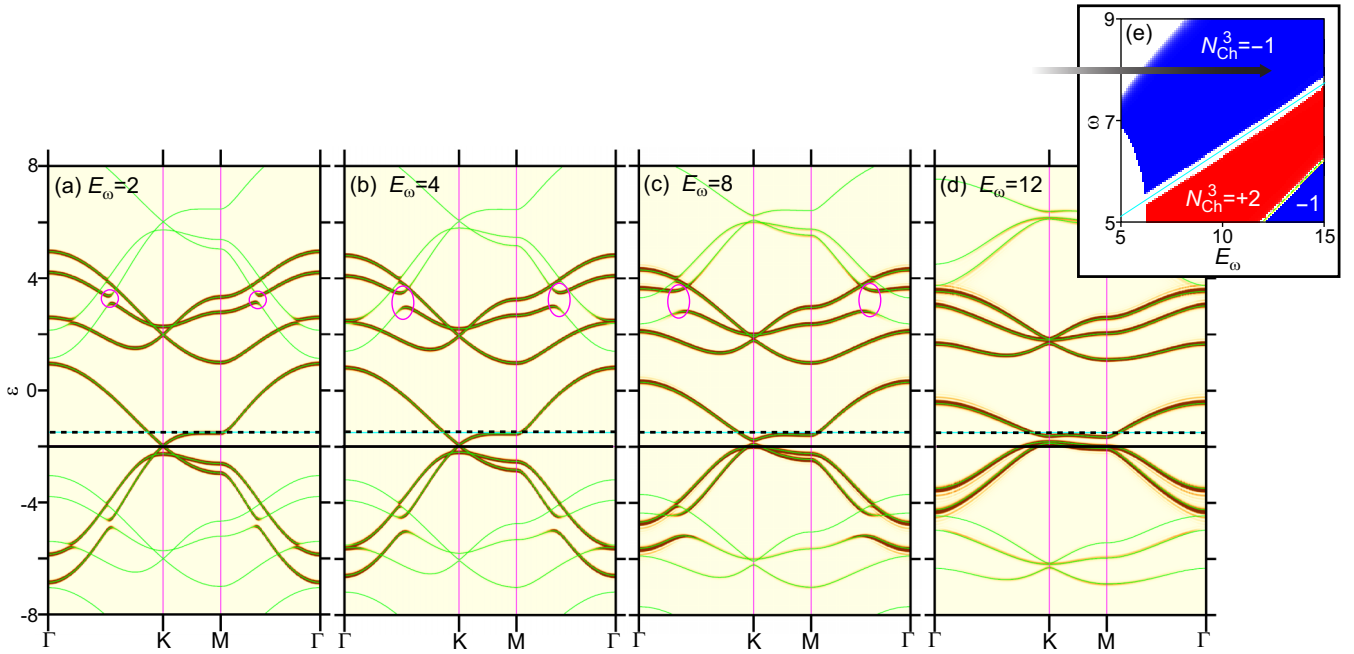


FIG. 4. (a)–(d) Single-particle spectra $A(\mathbf{q}, \varepsilon)$ for various values of E_ω , i.e., (a) $E_\omega = 2$, (b) $E_\omega = 4$, (c) $E_\omega = 8$, and (d) $E_\omega = 12$, respectively, when $\omega = 8$. The horizontal solid lines represent the energy level of Dirac points at K point in equilibrium, while the horizontal dashed lines represent the chemical potential ($\mu = -1.5$) used in the present simulations. (e) Variation of E_ω from (a) to (d) is indicated by a horizontal thick arrow.

sidebands are partially occupied by electrons. On the contrary, there are some points at which band crossing instead of anti-crossing occurs. At these band-crossing points, the spectral weight $A(\mathbf{q}, \varepsilon)$ does not exhibit particular change or anomaly. The crossing and anticrossing of the bands are governed by the structure of the Hamiltonian matrix. The Hamiltonian matrix $\mathcal{H}_{\text{IKLM}}$ can be block-diagonalized into independent up-spin and down-spin blocks as $\mathcal{H}_{\text{IKLM}} = \mathcal{H}_\uparrow \oplus \mathcal{H}_\downarrow$. When two bands belong to the same (different) spin blocks, the anticrossing (crossing) occurs when they cross.

Next we discuss the variation of band structures upon another topological phase transition, which occurs from the $N_{\text{Ch}} = +1$ phase to the $N_{\text{Ch}} = -2$ phase with decreasing ω when E_ω is fixed at 12. Figure 5(a) indicates that both K and M points are gapped when $\omega = 7.5$, and the system has a Chern number of $N_{\text{Ch}} = +1$ associated with the photoinduced gapped Dirac point at the K point. As ω decreases, the band gap at the M point gradually decreases. Indeed, as seen in Figs. 5(b) and 5(c), the band gap at the M point is almost closed when $\omega = 7$ and $\omega = 6.8$. With further decreasing ω , the band gap starts opening again after the system enters the $N_{\text{Ch}} = -2$ phase. As seen in Fig. 5(d), a clear gap opens up when $\omega = 6$.

The Chern number of $N_{\text{Ch}} = -2$ in the system after the gap reopening at the M point can be understood as follows. First, the Dirac-gap opening at the K point gives the Chern number of $+1$ to the lowest two bands, i.e., $N_{\text{Ch}}^1 + N_{\text{Ch}}^2 = +1$. Subsequently, the closing and reopening of gap at the M points give additional Chern number of -1 at each M point. Because the system has three independent M points in the hexagonal Brillouin zone of the up-up-down ferrimagnetic order, the total Chern number becomes $N_{\text{Ch}} = (+1) + (-1) \times 3 = -2$.

C. Hall conductivity

It is predicted that these two Floquet Chern insulator phases in the photodrive ferrimagnetic system can be detected and distinguished experimentally by the measurement of Hall conductivity σ_{xy} . Figure 6(a) shows the E_ω dependence of σ_{xy} calculated using the Keldysh Green's-function formalism when ω is fixed at 8. Here, Fig. 6(b) shows the calculated chemical potential μ when the electron filling is $n_e = 0.34$. In Fig. 6(a), we find that σ_{xy} is almost zero when E_ω is as small as $E_\omega \lesssim 4$. As E_ω increases, σ_{xy} increases gradually. When $E_\omega \sim 12$ inside the $N_{\text{Ch}} = 1$ phase, σ_{xy} is nearly quantized to e^2/h at a low temperature of $T = 23$ K, which corresponds to the Chern number of $N_{\text{Ch}} = +1$ in the Floquet Chern insulator phase I. Such a quantization of σ_{xy} cannot be seen at a higher temperature of $T = 300$ K. However, we still observe a positive nonzero σ_{xy} as large as 20% of the quantized value at $T = 300$ K.

On the other hand, Figs. 6(c) and 6(d) show the ω -dependence of σ_{xy} and μ when E_ω is fixed at 12. We find that nearly-quantized values of σ_{xy} of $-2e^2/h$ and e^2/h are observed in the two Floquet Chern insulator phases with $N_{\text{Ch}} = -2$ and $N_{\text{Ch}} = +1$, respectively, at low temperatures ($T = 23$ K), whereas the quantization is obscure at higher temperatures ($T = 300$ K). A clear sign change of σ_{xy} from negative to positive is observed when the system enters from the $N_{\text{Ch}} = -2$ phase to the $N_{\text{Ch}} = +1$ phase with increasing ω . Interestingly, this sign change is observed not only at $T = 23$ K but also at $T = 300$ K. Moreover, Fig. 6(e) indicates that the sign change survives even at 900 K. The heating is unavoidable in real experiments with light irradiation, but this result indicates that the sign change is robust against rise in

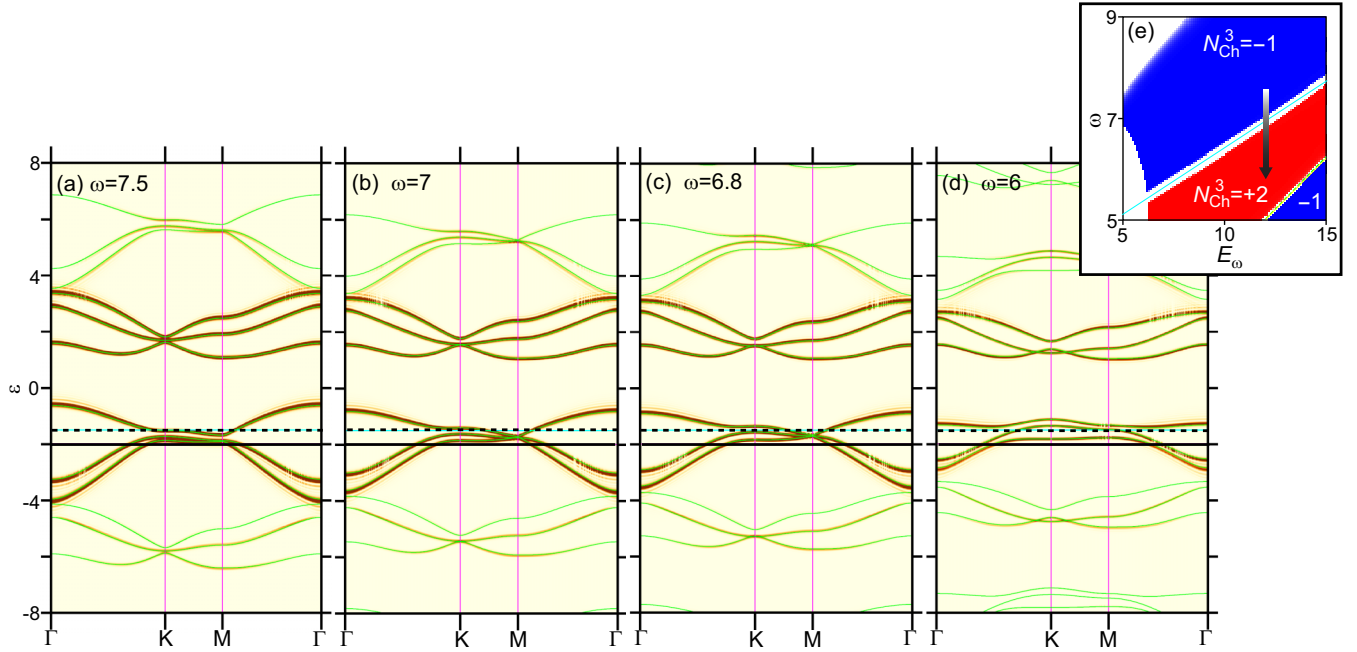


FIG. 5. (a)–(d) Single-particle spectra $A(\mathbf{q}, \varepsilon)$ for various values of ω , i.e., (a) $\omega = 7.5$ (b) $\omega = 7$, (c) $\omega = 6.8$, and (d) $\omega = 6$, respectively, when $E_\omega = 12$. The horizontal solid lines represent the energy level of Dirac points at K point in equilibrium, while the horizontal dashed lines represent the chemical potential ($\mu = -1.5$) used in the present simulations. (e) Variation of ω from (a) to (d) is indicated by a vertical thick arrow.

temperature, which is a favorable property for the experimental observation.

In Fig. 6(c), we can find that the quantization of the Hall currents are more pronounced in the $N_{\text{Ch}} = +1$ regions compared to the $N_{\text{Ch}} = -2$ regions at low temperatures. One possible scenario to describe the reason of the difference in quantization is the difference in nonequilibrium band structures between the $N_{\text{Ch}} = +1$ phase and the $N_{\text{Ch}} = -2$ phase. In fact, Figs. 3(a) and 3(b) indicate that the indirect bandgap Δ_{23} is positive for most of the $N_{\text{Ch}} = +1$ regions while it is negative for most of the $N_{\text{Ch}} = -2$ regions. Considering that the negative indirect bandgap makes the quantized Hall signatures obscure, it makes sense that the quantization of the Hall currents in $N_{\text{Ch}} = -2$ is less pronounced than those in $N_{\text{Ch}} = +1$.

D. Analyses based on the high-frequency expansion

As discussed in Sec. III C, the Floquet engineering has often been performed using the effective Floquet Hamiltonian obtained by the Brillouin-Wigner expansion in the high-frequency limit. More specifically, Hamiltonians composed of up to the first-order terms of the expansion with respect to $1/\omega$ have been frequently used for the research. However, it is known that the first-order terms usually vanish because of the cancellation of equivalent paths having phases with opposite signs. In multipartite lattices, we can avoid this cancellation to obtain a nonzero contribution from the first-order terms. On the contrary, the cancellation cannot be avoided in simple lattices such as square and triangular lattices even in the presence of extrinsic sublattice degrees of freedom introduced by long-range orders of spins and/or charges. Thereby,

Floquet topological electron states and photoinduced topological phase transition cannot be expected in electron systems on simple lattices within the crude approximation based on the high-frequency expansion up to the first-order. This is a reason why several multipartite lattices such as Kagome lattices, honeycomb lattices, and Lieb lattices have been studied in the research of Floquet engineering, whereas simple square lattices and triangular lattices have not been in a scope of the research.

However, as discussed above, we have obtained rich Floquet Chern insulator phases in the triangular Kondo-lattice model by the analyses based on direct diagonalization of the truncated effective Floquet Hamiltonian. In the present system, a ferrimagnetic order has been assumed to realize the Dirac-cone bands around the K point. The above-argued cancellation of the first-order terms also occurs even in the presence of sublattice degrees of freedom due to the ferrimagnetic spin order. In fact, the Floquet Chern insulator phases in the present triangular-lattice system are attributable to the higher-order terms of the expansion.

To demonstrate the substantial role of the higher-order terms, we calculate the band structure around the K point under irradiation with circularly polarized light when $E_\omega = 6$ and $\omega = 6$. Figure 7(a) shows the band structure calculated using a Hamiltonian matrix composed of up to the first-order terms only, that is, $\hat{H}_{\text{BW}} = \hat{H}_{\text{BW}}^{(0)} + \hat{H}_{\text{BW}}^{(1)}$. This band structure is nearly the same with that in equilibrium without photoirradiation in Fig. 1(c), because the zeroth-order term $\hat{H}_{\text{BW}}^{(0)}$ corresponds to the time-averaged Hamiltonian and the first-order term $\hat{H}_{\text{BW}}^{(1)}$ vanishes due to the perfect cancellation.

In Fig. 7(b), we show the band structure calculated using a Hamiltonian matrix including up to the second-order terms,

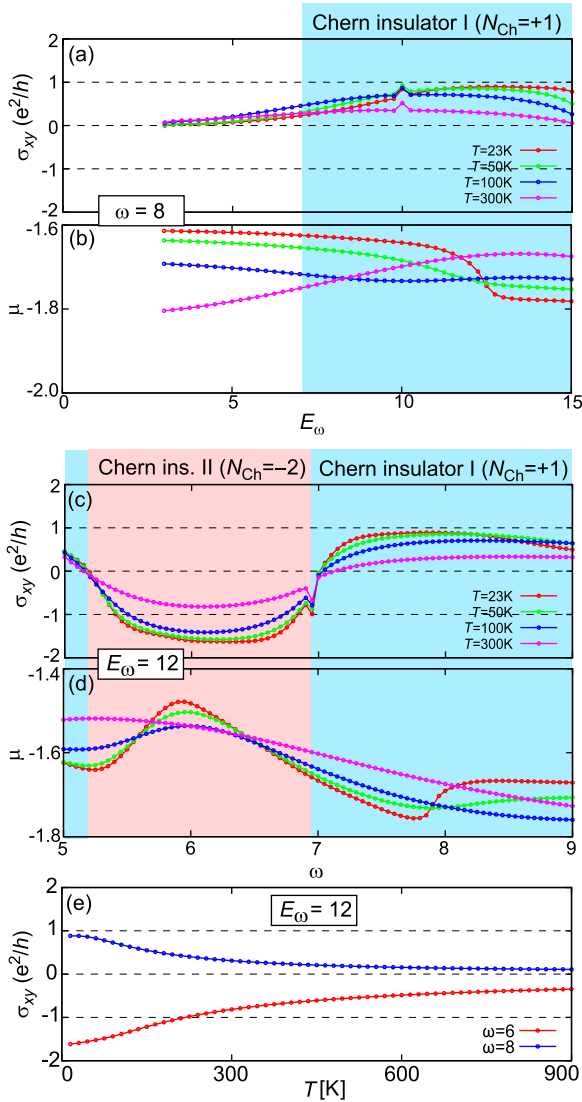


FIG. 6. (a) Hall conductivity σ_{xy} and (b) Chemical potential μ for the electron filling of $n_e = 0.34$ in the photodriven system as functions of E_ω when $\omega = 8$. (c), (d) Those as functions of ω when $E_\omega = 12$. (e) σ_{xy} as a function of temperature when $E_\omega = 12$ and $\omega = 6, 8$.

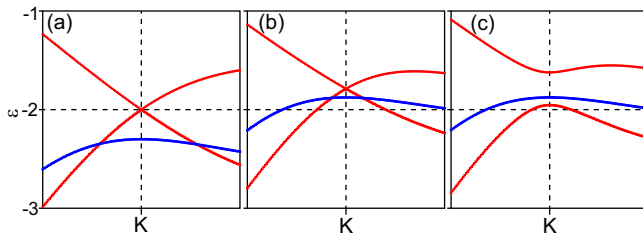


FIG. 7. Contributions from terms of the high-frequency expansion (the Brillouin-Wigner expansion) to the Floquet-band structure in the photoradiated system. The band dispersion relations around the K point are calculated using the Brillouin-Wigner Hamiltonian \hat{H}_{BW} in Eq. (42) up to (a) the first-, (b) the second-, and (c) the third-order terms with respect to $1/\omega$ when $E_\omega = 6$ and $\omega = 6$.

that is, $\hat{H}_{BW} = \sum_{n=0}^2 \hat{H}_{BW}^{(n)}$. The overall band structure shifts upward along the energy axis, indicating that the second-order term $\hat{H}_{BW}^{(2)}$ has a nonzero contribution, but it cannot open a gap at the Dirac point. The band structure calculated for $\hat{H}_{BW} = \sum_{n=0}^3 \hat{H}_{BW}^{(n)}$ in Fig. 7(c), in contrast, shows a gapped Dirac point. This indicates that the third-order term $\hat{H}_{BW}^{(3)}$ is the lowest-order term required to open a gap at the Dirac point. Owing to this gap opening, the system attains a nonzero Chern number of $N_{Ch} = +1$.

These results clearly demonstrate that the higher-order terms of the Brillouin-Wigner expansion instead of the usually considered first-order terms are relevant to the gap opening at the Dirac point, which results in the photoinduced topological phase transition and rich Floquet topological phases. This aspect is expected to widen the target materials of the Floquet engineering and to enhance the possibility of the research.

V. SUMMARY

As we discussed earlier in this paper, the main targets of the Floquet engineering have been the multipartite lattices, e.g., honeycomb, Kagome, and Lieb lattices in which the sublattice degrees of freedom are coming only from lattice geometry, in other words, originally imprinted even without considering spin or orbital degrees of freedom of electrons. We here have demonstrated that such “lattice geometry-induced” or “originally imprinted” sublattice degrees of freedom are not necessarily required for the Floquet engineering and it could be done even in the monopartite systems, as long as they have “non-imprinted” sublattice degrees of freedom induced by the spontaneous orderings of spins (or even orbitals). In the latter case, not the lowest but higher-order terms in the high-frequency expansion give us the feasibility of the Floquet engineering.

More specifically, as a typical example of the latter case, we have theoretically studied the effects of photoirradiation with circularly polarized light on the Dirac half-metal state in the triangular Kondo-lattice model with a three-sublattice ferrimagnetic order. By applying the Floquet analysis based on the truncated Floquet Hamiltonian, we have found that two types of Floquet Chern insulator phases with distinct Chern numbers of $N_{Ch} = +1$ and $N_{Ch} = -2$ appear as nonequilibrium steady states, which originate from the band gap formation/closing at distinct momentum points. By calculating the Hall conductivity in the photodriven system using the Keldysh Green’s function formalism, we have revealed that these two Floquet Chern insulator phases can be experimentally detected and are distinguishable by measurements of the Hall conductivity. Specifically, it has been revealed that the Hall conductivity takes nearly quantized values of e^2/h and $-2e^2/h$ with opposite signs in the respective phases. It has also been elucidated that these nonequilibrium topological phases come from the higher-order terms in the Brillouin-Wigner expansion in the high-frequency limit, which is in striking contrast to usually discussed Floquet Chern insulator phases originating from the lowest-order terms of the expansion. Because the first-order terms generally cancel out

and vanish in simple nonmultipartite lattices, research of the Floquet engineering has been performed by taking several multipartite lattices, e.g., the Kagome lattices, the honeycomb lattices, and the Lieb lattices. However, the present work has revealed that the higher-order terms, which have nonzero contributions even in the nonmultipartite lattices, can induce the photoinduced topological phase transitions and the Floquet topological electron phases. This aspect indicates that various lattice electron models on simple lattices such as square lattices and triangular lattices can also be within a scope of the Floquet engineering. We expect that the predicted Floquet Chern insulator phases might be observed in triangular ferrimagnets $R\text{Fe}_2\text{O}_4$ ($R = \text{Yb}, \text{Lu}, \text{Er}$) [58–61] under irradiation with circularly polarized light. The present work will widen the list of candidate target materials/systems for the

Floquet engineering and enhance the possibility of research in this field.

ACKNOWLEDGMENTS

R.E. is grateful to A. Ono for useful discussion. This work was supported by the Japan Science and Technology Agency, CREST (Grant No. JPMJCR20T1), JSPS KAKENHI (Grants No. JP20H00337, No. JP23H04522, and No. 24H02231), and Waseda University Grant for Special Research (Projects No. 2023C-140 and No. 2024C-153). R.E. was supported by a Grant-in-Aid for JSPS Fellows (Grant No. 23KJ2047). Numerical calculations were in part performed at the Supercomputer Center, Institute for Solid State Physics, University of Tokyo.

-
- [1] T. Oka and H. Aoki, Photovoltaic Hall effect in graphene, *Phys. Rev. B* **79**, 081406(R) (2009).
- [2] T. Kitagawa, T. Oka, A. Brataas, L. Fu, and E. Demler, Transport properties of nonequilibrium systems under the application of light: Photoinduced quantum Hall insulators without Landau levels, *Phys. Rev. B* **84**, 235108 (2011).
- [3] T. Oka and S. Kitamura, Floquet engineering of quantum materials, *Annu. Rev. Condens. Matter Phys.* **10**, 387 (2019).
- [4] A. de la Torre, D. M. Kennes, M. Claassen, S. Gerber, J. W. McIver, and M. A. Sentef, *Colloquium*: Nonthermal pathways to ultrafast control in quantum materials, *Rev. Mod. Phys.* **93**, 041002 (2021).
- [5] J. W. McIver, B. Schulte, F.-U. Stein, T. Matsuyama, G. Jotzu, G. Meier, and A. Cavalleri, Light-induced anomalous Hall effect in graphene, *Nat. Phys.* **16**, 38 (2020).
- [6] S. A. Sato, J. W. McIver, M. Nuske, P. Tang, G. Jotzu, B. Schulte, H. Hübener, U. De Giovannini, L. Mathey, M. A. Sentef, A. Cavalleri, and A. Rubio, Microscopic theory for the light-induced anomalous Hall effect in graphene, *Phys. Rev. B* **99**, 214302 (2019).
- [7] G. E. Topp, G. Jotzu, J. W. McIver, L. Xian, A. Rubio, and M. A. Sentef, Topological Floquet engineering of twisted bilayer graphene, *Phys. Rev. Res.* **1**, 023031 (2019).
- [8] M. Rodriguez-Vega, M. Vogl, and G. A. Fiete, Floquet engineering of twisted double bilayer graphene, *Phys. Rev. Res.* **2**, 033494 (2020).
- [9] I. A. Assi, J. P. F. LeBlanc, M. Rodriguez-Vega, H. Bahlouli, and M. Vogl, Floquet engineering and nonequilibrium topological maps in twisted trilayer graphene, *Phys. Rev. B* **104**, 195429 (2021).
- [10] M. Ezawa, Photoinduced topological phase transition and a single Dirac-cone state in silicene, *Phys. Rev. Lett.* **110**, 026603 (2013).
- [11] Y. Kang, S.-Y. Park, and K. Moon, Photoinduced topological phase transition and optical conductivity of black phosphorene, *Phys. Rev. B* **101**, 035137 (2020).
- [12] M. Claassen, C. Jia, B. Moritz, and T. P. Devereaux, All-optical materials design of chiral edge modes in transition-metal dichalcogenides, *Nat. Commun.* **7**, 13074 (2016).
- [13] M. Y. Zhang, Z. X. Wang, Y. N. Li, L. Y. Shi, D. Wu, T. Lin, S. J. Zhang, Y. Q. Liu, Q. M. Liu, J. Wang, T. Dong, and N. L. Wang, Light-induced subpicosecond lattice symmetry switch in MoTe_2 , *Phys. Rev. X* **9**, 021036 (2019).
- [14] H. Chono, K. Takasan, and Y. Yanase, Laser-induced topological s -wave superconductivity in bilayer transition metal dichalcogenides, *Phys. Rev. B* **102**, 174508 (2020).
- [15] M. Vogl, M. Rodriguez-Vega, B. Flebus, A. H. MacDonald, and G. A. Fiete, Floquet engineering of topological transitions in a twisted transition metal dichalcogenide homobilayer, *Phys. Rev. B* **103**, 014310 (2021).
- [16] K. Kitayama and M. Mochizuki, Predicted photoinduced topological phases in organic salt α -(BEDT-TTF) $_2\text{I}_3$, *Phys. Rev. Res.* **2**, 023229 (2020).
- [17] K. Kitayama, M. Mochizuki, Y. Tanaka, and M. Ogata, Predicted photoinduced pair annihilation of emergent magnetic charges in the organic salt α -(BEDT-TTF) $_2\text{I}_3$ irradiated by linearly polarized light, *Phys. Rev. B* **104**, 075127 (2021).
- [18] K. Kitayama, Y. Tanaka, M. Ogata, and M. Mochizuki, Floquet theory of photoinduced topological phase transitions in the organic salt α -(BEDT-TTF) $_2\text{I}_3$ irradiated with elliptically polarized light, *J. Phys. Soc. Jpn.* **90**, 104705 (2021).
- [19] K. Kitayama, M. Ogata, M. Mochizuki, and Y. Tanaka, Predicted novel type of photoinduced topological phase transition accompanied by collision and collapse of Dirac-cone pair in organic salt α -(BEDT-TTF) $_2\text{I}_3$, *J. Phys. Soc. Jpn.* **91**, 104704 (2022).
- [20] K. Kitayama and M. Ogata, Nonlinear optical response in multi-band Dirac-electron system, *Phys. Rev. B* **110**, 045127 (2024).
- [21] Y. Tanaka and M. Mochizuki, Real-time dynamics of the photoinduced topological state in the organic conductor α -(BEDT-TTF) $_2\text{I}_3$ under continuous-wave and pulse excitations, *Phys. Rev. B* **104**, 085123 (2021).
- [22] Y. Tanaka and M. Mochizuki, Dynamical phase transitions in the photodriven charge-ordered Dirac-electron system, *Phys. Rev. Lett.* **129**, 047402 (2022).
- [23] K. Takasan, A. Daido, N. Kawakami, and Y. Yanase, Laser-induced topological superconductivity in cuprate thin films, *Phys. Rev. B* **95**, 134508 (2017).
- [24] M. S. Rudner, N. H. Lindner, E. Berg, and M. Levin, Anomalous edge states and the bulk-edge correspondence for periodically driven two-dimensional systems, *Phys. Rev. X* **3**, 031005 (2013).

- [25] P. M. Perez-Piskunow, G. Usaj, C. A. Balseiro, and L. E. F. Foa Torres, Floquet chiral edge states in graphene, *Phys. Rev. B* **89**, 121401(R) (2014).
- [26] G. Usaj, P. M. Perez-Piskunow, L. E. F. Foa Torres, and C. A. Balseiro, Irradiated graphene as a tunable Floquet topological insulator, *Phys. Rev. B* **90**, 115423 (2014).
- [27] R. Roy and F. Harper, Periodic table for Floquet topological insulators, *Phys. Rev. B* **96**, 155118 (2017).
- [28] A. G. Grushin, Á. Gómez-León, and T. Neupert, Floquet fractional Chern insulators, *Phys. Rev. Lett.* **112**, 156801 (2014).
- [29] M. Schüler, U. De Giovannini, H. Hübener, A. Rubio, M. A. Sentef, T. P. Devereaux, and P. Werner, How circular dichroism in time- and angle-resolved photoemission can be used to spectroscopically detect transient topological states in graphene, *Phys. Rev. X* **10**, 041013 (2020).
- [30] M. Schüler and S. Beaulieu, Probing topological Floquet states in WSe₂ using circular dichroism in time- and angle-resolved photoemission spectroscopy, *Commun. Phys.* **5**, 164 (2022).
- [31] M. S. Rudner and N. H. Lindner, Band structure engineering and non-equilibrium dynamics in Floquet topological insulators, *Nat. Rev. Phys.* **2**, 229 (2020).
- [32] Y. H. Wang, H. Steinberg, P. Jarillo-Herrero, and N. Gedik, Observation of Floquet-Bloch states on the surface of a topological insulator, *Science* **342**, 453 (2013).
- [33] S. Ito, M. Schüler, M. Meierhofer, S. Schlauderer, J. Freudenstein, J. Reimann, D. Afanasiev, K. A. Kokh, O. E. Tereshchenko, J. Güdde, M. A. Sentef, U. Höfer, and R. Huber, Build-up and dephasing of Floquet-Bloch bands on subcycle timescales, *Nature (London)* **616**, 696 (2023).
- [34] R. Wang, B. Wang, R. Shen, L. Sheng, and D. Y. Xing, Floquet Weyl semimetal induced by off-resonant light, *Europhys. Lett.* **105**, 17004 (2014).
- [35] S. Ebihara, K. Fukushima, and T. Oka, Chiral pumping effect induced by rotating electric fields, *Phys. Rev. B* **93**, 155107 (2016).
- [36] H. Hübener, M. A. Sentef, U. De Giovannini, A. F. Kemper, and A. Rubio, Creating stable Floquet-Weyl semimetals by laser-driving of 3D Dirac materials, *Nat. Commun.* **8**, 13940 (2017).
- [37] G. E. Topp, N. Tancogne-Dejean, A. F. Kemper, A. Rubio, and M. A. Sentef, All-optical nonequilibrium pathway to stabilising magnetic Weyl semimetals in pyrochlore iridates, *Nat. Commun.* **9**, 4452 (2018).
- [38] N. Tsuji, T. Oka, and H. Aoki, Correlated electron systems periodically driven out of equilibrium: Floquet+DMFT formalism, *Phys. Rev. B* **78**, 235124 (2008).
- [39] H. Aoki, N. Tsuji, M. Eckstein, M. Kollar, T. Oka, and P. Werner, Nonequilibrium dynamical mean-field theory and its applications, *Rev. Mod. Phys.* **86**, 779 (2014).
- [40] N. Tsuji, T. Oka, P. Werner, and H. Aoki, Dynamical band flipping in fermionic lattice systems: An ac-field-driven change of the interaction from repulsive to attractive, *Phys. Rev. Lett.* **106**, 236401 (2011).
- [41] Y. Murakami, M. Eckstein, and P. Werner, High-harmonic generation in Mott insulators, *Phys. Rev. Lett.* **121**, 057405 (2018).
- [42] S. Takayoshi, H. Aoki, and T. Oka, Magnetization and phase transition induced by circularly polarized laser in quantum magnets, *Phys. Rev. B* **90**, 085150 (2014).
- [43] Y. Tanaka, T. Inoue, and M. Mochizuki, Theory of the inverse Faraday effect due to the Rashba spin-orbit interactions: Roles of band dispersions and Fermi surfaces, *New J. Phys.* **22**, 083054 (2020).
- [44] M. Sato, S. Takayoshi, and T. Oka, Laser-driven multiferroics and ultrafast spin current generation, *Phys. Rev. Lett.* **117**, 147202 (2016).
- [45] A. Ono and S. Ishihara, Double-exchange interaction in optically induced nonequilibrium state: A conversion from ferromagnetic to antiferromagnetic structure, *Phys. Rev. Lett.* **119**, 207202 (2017).
- [46] A. Ono and S. Ishihara, Photocontrol of magnetic structure in an itinerant magnet, *Phys. Rev. B* **98**, 214408 (2018).
- [47] T. Mikami, S. Kitamura, K. Yasuda, N. Tsuji, T. Oka, and H. Aoki, Brillouin-Wigner theory for high-frequency expansion in periodically driven systems: Application to Floquet topological insulators, *Phys. Rev. B* **93**, 144307 (2016).
- [48] Y. Ikeda, S. Kitamura, and T. Morimoto, Photocurrent induced by a bicircular light drive in centrosymmetric systems, *Phys. Rev. Lett.* **131**, 096301 (2023).
- [49] H. Ishizuka and Y. Motome, Dirac half-metal in a triangular ferrimagnet, *Phys. Rev. Lett.* **109**, 237207 (2012).
- [50] M. S. Rudner and N. H. Lindner, The Floquet engineer's handbook, [arXiv:2003.08252](https://arxiv.org/abs/2003.08252).
- [51] N. Tsuji, T. Oka, and H. Aoki, Nonequilibrium steady state of photoexcited correlated electrons in the presence of dissipation, *Phys. Rev. Lett.* **103**, 047403 (2009).
- [52] S. Rahav, I. Gilary, and S. Fishman, Effective Hamiltonians for periodically driven systems, *Phys. Rev. A* **68**, 013820 (2003).
- [53] J. Hausinger and M. Grifoni, Dissipative two-level system under strong ac driving: A combination of Floquet and Van Vleck perturbation theory, *Phys. Rev. A* **81**, 022117 (2010).
- [54] N. Goldman and J. Dalibard, Periodically driven quantum systems: Effective Hamiltonians and engineered gauge fields, *Phys. Rev. X* **4**, 031027 (2014).
- [55] A. Eckardt and E. Anisimovas, High-frequency approximation for periodically driven quantum systems from a Floquet-space perspective, *New J. Phys.* **17**, 093039 (2015).
- [56] J. K. Freericks, H. R. Krishnamurthy, and T. Pruschke, Theoretical description of time-resolved photoemission spectroscopy: Application to pump-probe experiments, *Phys. Rev. Lett.* **102**, 136401 (2009).
- [57] M. A. Sentef, M. Claassen, A. F. Kemper, B. Moritz, T. Oka, J. K. Freericks, and T. P. Devereaux, Theory of Floquet band formation and local pseudospin textures in pump-probe photoemission of graphene, *Nat. Commun.* **6**, 7047 (2015).
- [58] M. Tanaka, H. Iwasaki, K. Siratori, and I. Shindo, Mössbauer study on the magnetic structure of YbFe₂O₄: A two-dimensional antiferromagnet on a triangular lattice, *J. Phys. Soc. Jpn.* **58**, 1433 (1989).
- [59] J. Iida, M. Tanaka, Y. Nakagawa, S. Funahashi, N. Kimizuka, and S. Takekawa, Magnetization and spin correlation of two-dimensional triangular antiferromagnet LuFe₂O₄, *J. Phys. Soc. Jpn.* **62**, 1723 (1993).
- [60] H. Kito, S. Isida, M. Suzuki, J. Akimitsu, S. Takekawa, and K. Siratori, Ultrasonic investigation of a two-dimensional triangular lattice ferrimagnet, ErFe₂O_{4-δ} single crystal, *J. Phys. Soc. Jpn.* **64**, 2147 (1995).
- [61] H. Kito, M. Nishi, S. Katano, J. Akimitsu, S. Funahashi, and K. Siratori, Interlayer spin correlation in a 2-D triangular ferrimagnet ErFe₂O₄, *J. Magn. Magn. Mater.* **140-144**, 1647 (1995).